AIAA JOURNAL
Vol. 47, No. 8, August 2009

New Dissipative Leapfrog Finite Difference Scheme for Elastodynamic Simulation in Noninertial Frames

Upender K. Kaul*
NASA Ames Research Center, Moffett Field, California 94035

DOI: 10.2514/1.41393

A new approach to numerically solving problems of the elastodynamics of arbitrarily shaped bodies with nonuniform material properties in rotation has been proposed in the present study. The present approach is based on first principles and is well suited to the study of problems of fluid–structure interaction and wave-based structural health monitoring. The governing hyperbolic partial differential equations of elastodynamics are cast in strong conservation form in the noninertial frame of reference and in generalized curvilinear coordinates. The results are obtained directly in the time domain. No special boundary treatment is required at material interfaces, and predictions can be made with and without material damage in a given structure for damage detection of the structure. The effect on the dynamics of a rotating annulus due to centrifugal force and, additionally, Coriolis force at high rates of rotation is studied. The partial differential equations are solved using a new dissipative time-centered leapfrog scheme presented here. A one-dimensional theoretical analysis of the numerical scheme shows that the new scheme has well-defined stability and dissipation characteristics. A comparison of the new scheme with a conventional dissipative time-centered leapfrog scheme shows that much larger time steps can be taken with the new scheme than allowed by the existing scheme. A dissipation-dependence study demonstrates that as the dissipation parameter is decreased, the steady-state solution uniformly approaches the exact solution. For larger values of this parameter, although the natural frequency of the system is not altered, the system vibrations damp too quickly, and the steady-state solution deviates from the exact steady-state solution. The larger the dissipation parameter, the larger this deviation from the exact steady state. The present scheme is very simple to incorporate in a finite difference simulation of elastodynamics in generalized curvilinear coordinates, and it has been used in the software FiDDLE, which solves the velocity-stress system of elastodynamic partial differential equations. It will be used in simulating fluid–elastodynamic interaction of the Mars Science Laboratory canopies and other decelerators such as inflatable aerodynamic devices as well as in wave-based structural health monitoring of these systems. Other applications include elastodynamics of turbomachinery blades, computer disk drive, and cutting-tool industry applications.

Nomenclature

C_p	=	dilatational wave speed, $\sqrt{((\lambda + 2\mu)/\rho)}$
C_s	=	distortional wave speed, $\sqrt{(\mu/\rho)}$
E	=	Young's modulus of elasticity
f	=	body force
J	=	Jacobian of coordinate transformation
q_i, Q	=	velocity vector
R	=	right-hand side terms
r	=	radius
u, v, w	=	velocity components
x, y, z, t	=	Cartesian coordinates and time coordinate
δ_{ij}	=	Kronecker delta
λ, μ	=	Lame constants
ξ, η, ζ, ϵ	=	generalized curvilinear coordinates and time coordinate
ρ	=	material density
σ	=	Poisson's ratio
τ	=	symmetric stress tensor
Ω	=	rotational speed

Subscripts

i, j, k	=	indices for coordinate directions

Superscript

T	=	vector transpose

I. Introduction

THE solution of elastodynamic partial differential equations by staggered-grid finite difference method became popular with the work of Virieux [1] and Madariaga [2]. Many such studies [1–5] were related to seismological applications. Subsequently, other finite difference simulation studies were reported in the literature (e.g., [6–11]). Most of these finite difference studies used the staggered-grid scheme [1–3] in Cartesian coordinates. To the author's knowledge, three-dimensional finite difference simulations of elastodynamics of nonhomogeneous bodies in generalized curvilinear coordinates using this staggered-grid approach was first reported by the author [12–14] in simulating gear vibrations. In flux-conservation form with nonuniform material properties and in generalized coordinates, the staggered-grid finite difference method becomes very involved. To solve such problems of elastodynamics of arbitrarily shaped bodies of nonuniform material properties using finite differences, a recourse to generalized curvilinear coordinates has to be made. It is with this motivation that the present study has been carried out, and this entails a simpler numerical scheme for the generalized coordinates, such as a time-centered leapfrog scheme with an appropriate dissipation term with proper damping and stability characteristics. Survey and use of such schemes in the literature [15] made it clear that a better scheme could be developed for our purpose. Thus, a new dissipative time-centered leapfrog scheme is proposed here that is shown to be clearly superior to the one reported in the literature (e.g., [15]), by a comparison of solution convergence histories for a typical test case. The results are obtained directly in the time domain. For nonhomogeneous bodies, no special boundary treatment is required at material

Received 3 October 2008; revision received 23 April 2009; accepted for publication 30 April 2009.

*NASA Advanced Supercomputing Division; upender.kaul@nasa.gov. Associate Fellow AIAA.

interfaces, and predictions can be made with and without material damage for damage detection of a given structure. The new dissipative leapfrog scheme has been incorporated in the elastodynamic solver FiDDLE [12,16] to compute the known two-dimensional exact steady-state solution for a rotating annulus by following the unsteady development in time to an eventual steady state. The solver FiDDLE uses an enhanced automated elliptic grid generation scheme [17,18] and can thus generate a structured computational grid over any arbitrary geometry. The rotating annulus case was chosen for simplicity because it easily mimics the effect of an internal pressure acting radially outward on any annular structure through the modeled centrifugal force, similar to the forces experienced by an inflatable aerodynamic decelerator or a canopy in flight. Also, the finite difference methodology presented here will be applied to structural health monitoring (SHM) [19–25] of such systems.

II. Governing Equations

The three-dimensional linear elastodynamic equations of motion describing the principle of momentum conservation and the constitutive equations governing the wave phenomena within an isotropic elastic body can be written as a system of nine equations: three for the velocities and six for the stresses [1–5], respectively. The velocity equations are given by

$$\rho \partial_t q_i = \partial_j \tau_{ij} + f_i \tag{1}$$

where the velocity vector $q_i = (u, v, w)$, the body force vector is given by $f_i = (f_x, f_y, f_z)$, and the symmetric stress tensor τ_{ij} has six distinct components. The stress tensor is expressed by the following tensorial equation:

$$\partial_t \tau_{ij} = \lambda \delta_{ij} \mathrm{div} Q + \mu(\partial_j q_i + \partial_i q_j) \tag{2}$$

where div Q is the divergence of the velocity vector $Q(q_i)$, δ_{ij} is the Kronecker delta, and λ and μ are the Lame constants. The elastic quantities μ and λ are functions of space for a nonhomogeneous body.

In the rotating frame of reference, the velocity equations (1) become [12,26,27]

$$\rho \partial_t q_i = \partial_j \tau_{ij} + \partial_i(|\Omega \times r|^2/2) + 2\epsilon_{ijk} q_j \omega_k + f_i \tag{3}$$

where $|\Omega|$ is a constant rotational speed ($\Omega = \omega_k$), $r = (x, y, z)$ is a positional vector, and the second and third terms on the right-hand side represent the centrifugal and Coriolis forces associated with the rotating frame of reference [26,27].

In generalized curvilinear coordinates, using the conservative formulation of Viviand [28], the governing equations (2) and (3) for the elastodynamic system can be shown [12,29] to assume the following flux-conservative form:

$$\begin{aligned}\partial_\epsilon (A/J) + \partial_\xi[(A/J)\xi_t - (1/J)(\xi_x B + \xi_y C + \xi_z D)] + \partial_\eta[(A/J)\eta_t \\ - (1/J)(\eta_x B + \eta_y C + \eta_z D)] + \partial_\zeta[(A/J)\zeta_t \\ - (1/J)(\zeta_x B + \zeta_y C + \zeta_z D)] = R/J\end{aligned} \tag{4}$$

where

$$A = [\rho u, \rho v, \rho w, \tau_{xx}, \tau_{xy}, \tau_{xz}, \tau_{yy}, \tau_{yz}, \tau_{zz}]^T$$

$$B = [\tau_{xx}, \tau_{xy}, \tau_{xz}, (\lambda + 2\mu)u, \mu v, \mu w, \lambda u, 0, \lambda u]^T$$

$$C = [\tau_{xy}, \tau_{yy}, \tau_{yz}, \lambda v, \mu u, 0, (\lambda + 2\mu)v, \mu w, \lambda v]^T$$

$$D = [\tau_{xz}, \tau_{yz}, \tau_{zz}, \lambda w, 0, \mu u, \lambda w, \mu v, (\lambda + 2\mu)w]^T$$

The Jacobian of the transformation, J, is given by $\partial(x, y, z)/\partial(\xi, \eta, \zeta)$, and the metric quantities ξ_t, ξ_x, etc., have their usual meanings. The right-hand side column vector R contains the centrifugal and Coriolis terms and additional terms containing spatial derivatives of the elastic constants for nonhomogeneous bodies.

III. Numerical Scheme

In the original paper by Virieux [1], the velocity-stress staggered-grid finite difference method was first proposed in Cartesian coordinates to simulate earthquake signatures. The same method was extended by the author in simulating gear vibrations by casting the elastodynamic equations in flux-conservation form in generalized curvilinear coordinates. However, the staggered finite difference method becomes very involved for flux-conservation form in generalized coordinates. Therefore, a new time-centered dissipative leapfrog scheme with an appropriate second-order dissipation term is proposed here to be used in a finite difference simulation of elastodynamics in generalized curvilinear coordinates in conservation form. The scheme is very simple to use and is second-order in time and space, and it integrates the velocity-stress system in generalized coordinates. The flux-conservation form is maintained to ensure proper capture of any discontinuities such as cracks in the elastic medium. Both the spatial derivatives and time derivative are discretized using central differences. The new second-order dissipation term that eliminates the mesh drifting (checkerboard) instability is shown to be superior to a conventional dissipation term [15].

To demonstrate the effectiveness of the new dissipation term used in the numerical scheme, we will consider a one-dimensional system, as follows.

Assuming that the material properties are constant in time and further that the density is uniform, the one-dimensional velocity-stress system in Cartesian coordinates can be written as

$$U_t = AU_x + BU + C$$

where

$$U = \begin{pmatrix} u_t \\ C_p u_x \end{pmatrix}$$

$$A = \begin{pmatrix} 0 & C_p \\ C_p & 0 \end{pmatrix}$$

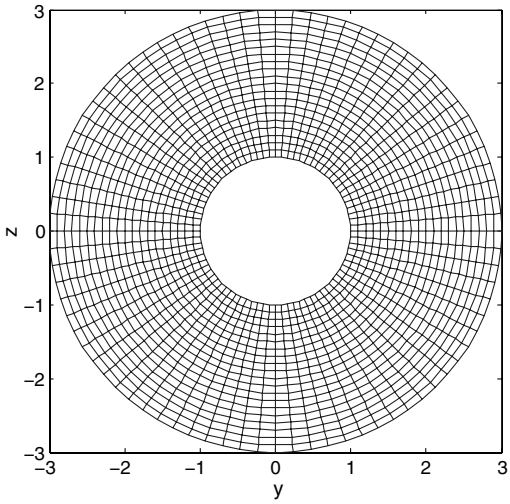

Fig. 1 Representative 80 × 21 grid of an annulus: 80 grid points in the circumferential direction and 21 points in the radial direction.

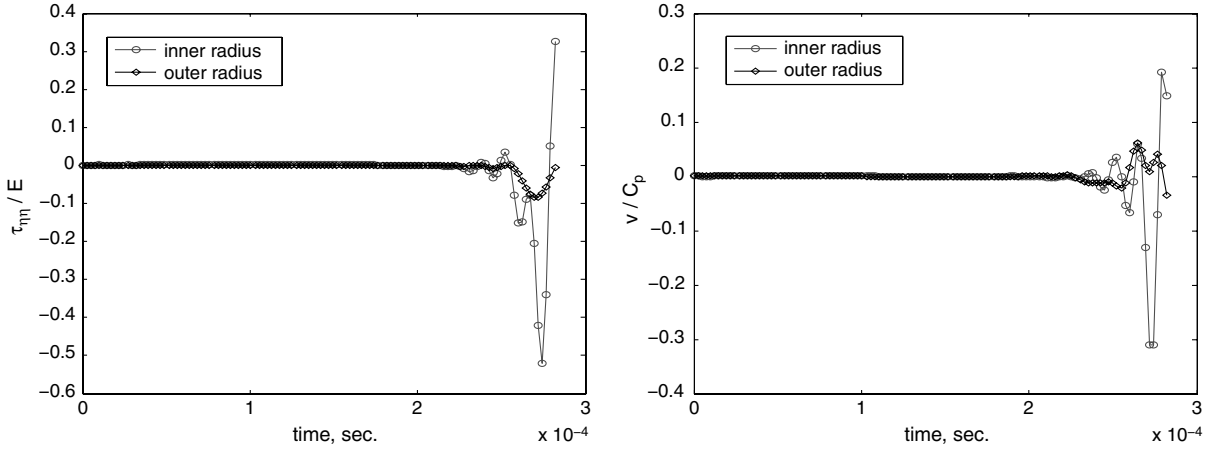

a) Tangential stress **b) Horizontal velocity**

Fig. 2 Time evolution at the inner and outer radii with the conventional scheme showing a rapid solution divergence; annulus rotating at 100 rps: a) $\tau_{\eta\eta}/E$ and b) v/C_p.

$$B = \begin{pmatrix} 0 & -C_{p_x} \\ 0 & 0 \end{pmatrix}$$

$$C = \begin{pmatrix} f_t/\rho \\ 0 \end{pmatrix}$$

A is symmetric and the system is symmetric hyperbolic, and therefore $\exists$ a real diagonal matrix Λ and an orthonormal matrix V subject to $A = V\Lambda V^T$. Therefore, we have

$$U_t = V\Lambda V^T U_x + BU + C$$

In general, for a real matrix A,

$$U_t = V\Lambda V^{-1} U_x + BU + C$$

The time-centered leapfrog scheme with the dissipation term used here is

$$U^{n+1} - U^{n-1} = 2\Delta t A\delta_0 U^n + 2\Delta t BU^n + 2\Delta t C + \epsilon(\Delta x)^2 \delta_+ \delta_- U^{n-1}$$

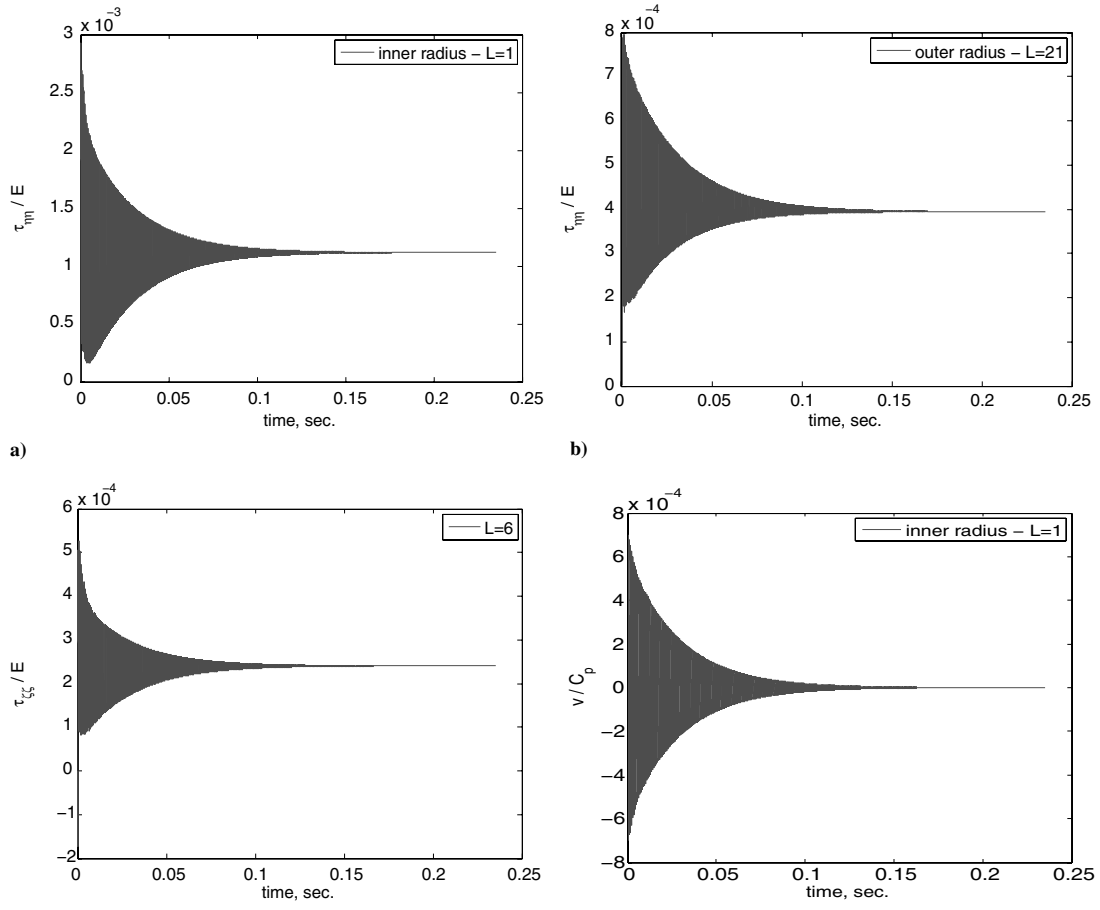

Fig. 3 Time evolution with the new scheme: annulus rotating at 100 rps; 80 × 21 grid: a–b) $\tau_{\eta\eta}$ evolution at two radial locations, c) $\tau_{\xi\xi}/E$ at $L = 6$, and d) v/C_p at the inner radius, $L = 1$.

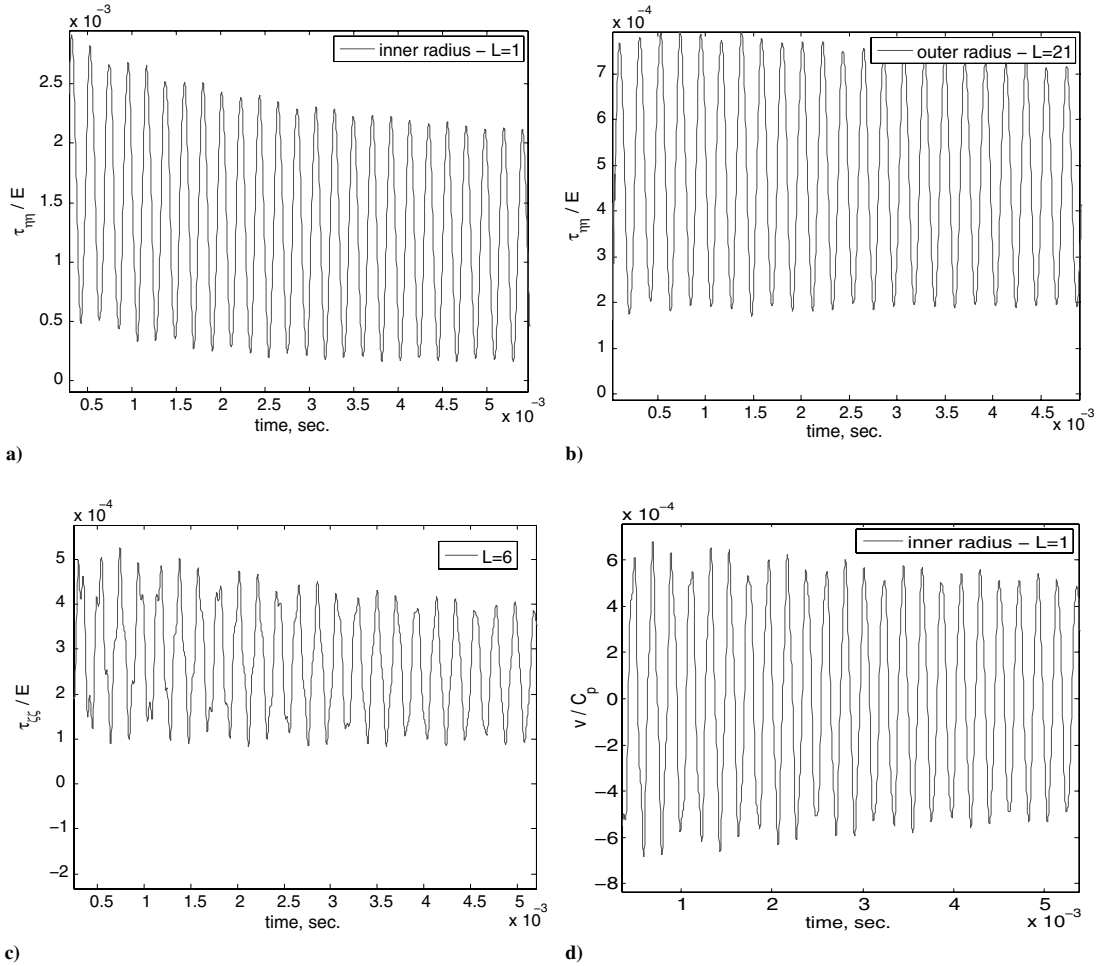

Fig. 4 Enlarged view of the time evolution with the new scheme showing a 5 KHz natural frequency response: annulus rotating at 100 rps; 80 × 21 grid: a–b) $\tau_{\eta\eta}$ evolution at two radial locations, c) $\tau_{\xi\xi}/E$ at $L = 6$, and d) v/C_p at the inner radius, $L = 1$.

where the central difference operators are given by

$$\delta_0 U = (U_{j+1} - U_{j-1})/(2\Delta x) \quad \text{and}$$
$$\delta_+\delta_- U = (U_{j+1} - 2U_j + U_{j-1})/\Delta x^2 \quad \text{and} \quad \epsilon \ll 1$$

Using Fourier representation for each Fourier component ψ of the solution, let

$$U_j = (1/2\pi)\int_{-\pi}^{\pi} e^{ij\psi}\tilde{U}(\psi)\mathrm{d}\psi$$

Ignoring time dependence of the conservative force field and the term containing B, the leapfrog system becomes

$$\begin{pmatrix} U^{n+1} \\ U^n \end{pmatrix} = \begin{pmatrix} 2\Delta t A\delta_0 & I + \epsilon(\Delta x)^2\delta_+\delta_- \\ I & 0 \end{pmatrix}\begin{pmatrix} U^n \\ U^{n-1} \end{pmatrix}$$

where I is a 2×2 identity matrix.

Setting $U_j = e^{ij\psi}$, the amplification matrix for this scheme is given by

$$G(\psi) = \begin{pmatrix} 2i(\Delta t/\Delta x)A\sin(\psi) & I - 4\epsilon\sin^2(\psi/2) \\ I & 0 \end{pmatrix}$$

Because $A = V\Lambda V^{-1}$, we can write the amplification matrix as

$$G(\psi) = \begin{pmatrix} V & 0 \\ 0 & V \end{pmatrix}\begin{pmatrix} 2i(\Delta t/\Delta x)\Lambda\sin(\psi) & I - 4\epsilon\sin^2(\psi/2) \\ I & 0 \end{pmatrix}$$
$$\begin{pmatrix} V^{-1} & 0 \\ 0 & V^{-1} \end{pmatrix}$$

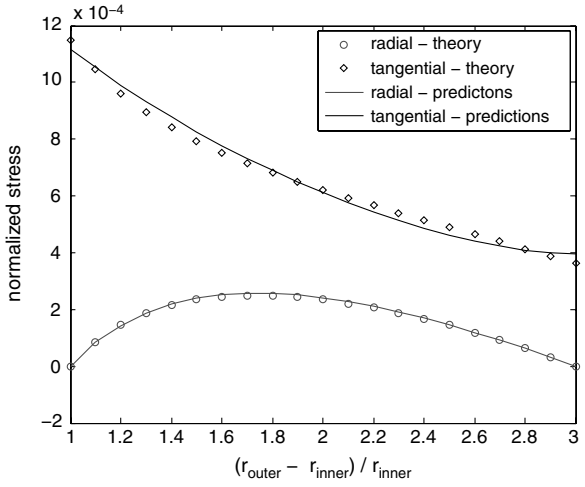

Fig. 5 Steady-state stress results for annulus rotating at 100 rps; comparison of predictions with 80 × 21 grid versus theoretical solution [30,31].

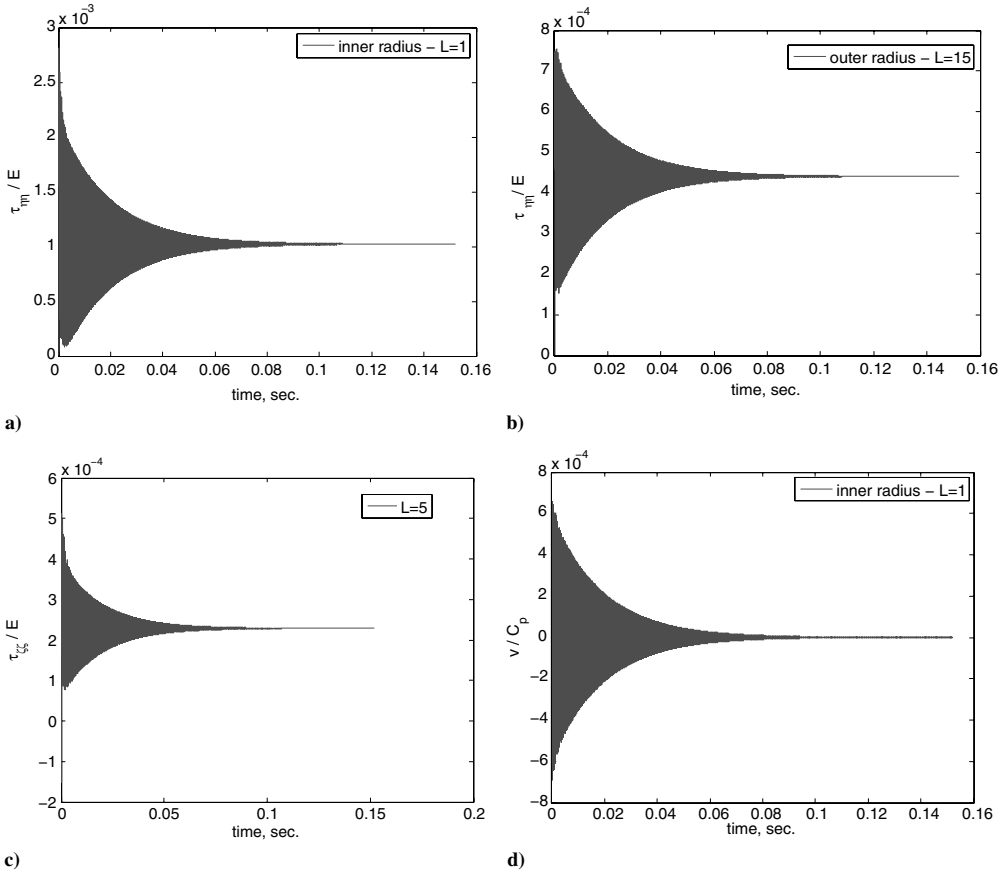

Fig. 6 Time evolution with the new scheme: annulus rotating at 100 rps; 60 × 15 grid: a–b) $\tau_{\eta\eta}/E$ evolution at two radial locations, c) $\tau_{\zeta\zeta}/E$ at $L = 5$, and d) v/C_p at the inner radius, $L = 1$.

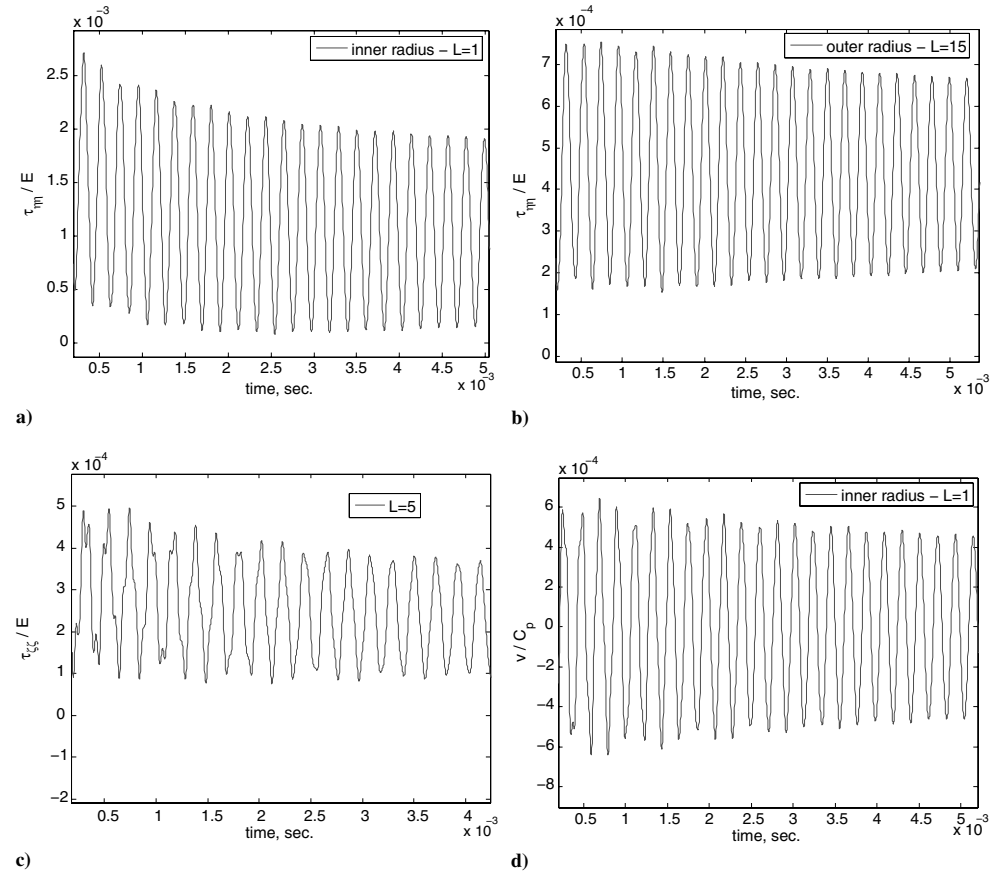

Fig. 7 Enlarged view of the time evolution with the new scheme showing a 5 KHz natural frequency response: annulus rotating at 100 rps; 60 × 15 grid: a–b) $\tau_{\eta\eta}/E$ evolution at two radial locations, c) $\tau_{\zeta\zeta}/E$ at $L = 5$, and d) v/C_p at the inner radius, $L = 1$.

Because Λ is a real diagonal matrix, the eigenvalue problem for G can be written as 2×2 block problems over the spatial index j. Thus, it is sufficient to treat the eigenvalue problem for the jth block, and the corresponding amplification matrix is given by

$$G_j(\psi) = \begin{pmatrix} 2i(\Delta t/\Delta x)\lambda_j \sin(\psi) & 1 - 4\epsilon \sin^2(\psi/2) \\ 1 & 0 \end{pmatrix}$$

The eigenvalues of this amplification matrix are given by

$$\chi = i(\Delta t/\Delta x)\lambda_j \sin(\psi) \pm \sqrt{(1 - 4\epsilon \sin^2(\psi/2) - (\Delta t/\Delta x)^2 \lambda_j^2 \sin^2(\psi)}$$

For $(\Delta t/\Delta x)^2 \lambda_j^2 \sin^2(\psi) < 1 - 4\epsilon \sin^2(\psi/2)$, we can write

$$|\chi|^2 = 1 - 4\epsilon \sin^2(\psi/2)$$

Thus, the scheme is dissipative and the stability criterion is given by

$$(\Delta t/\Delta x) \max_j |\lambda_j| < 1 - 2\epsilon$$

where $\lambda_j = \pm C_p$.

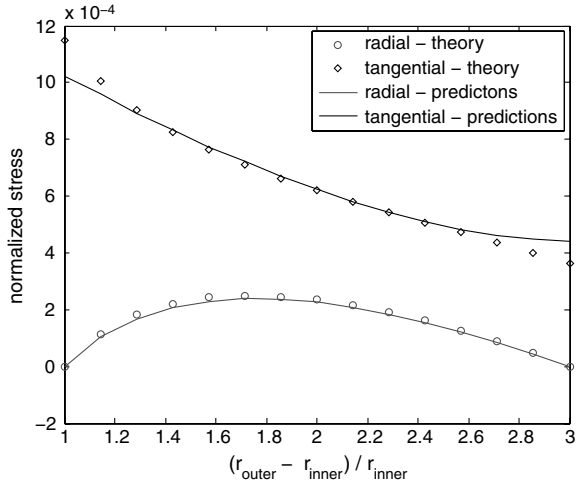

Fig. 8 Steady-state stress results for annulus rotating at 100 rps; comparison of predictions with 60 × 15 grid versus theoretical solution [30,31].

IV. Boundary Conditions

Fully characteristics boundary conditions have been formulated to prescribe the boundary conditions on velocities and stresses, as follows. Equation (4) in a two-dimensional (y, z) or (η, ζ) system can be written as

$$\partial_\tau A = M' A_\zeta + L' A_\eta + R \tag{4a}$$

where M' and L' are matrices containing the material properties and various metric quantities, and R is the term containing body forces and any traction by way of boundary conditions. Equation (4a) can further be written as

$$\partial_\tau A = U \Lambda U^{-1} A_\zeta + L' A_\eta + R \tag{4b}$$

or as

$$\partial_\tau A = UX + L' A_\eta + R \tag{4c}$$

where

$$X = \Lambda U^{-1} A_\zeta$$

is a vector of two incoming characteristics, two outgoing characteristics, and one neutral characteristic, corresponding to the zero eigenvalue of the matrix M'.

Therefore, on the boundaries, the solution variables are thus expressed in terms of these characteristics. Boundary conditions $\tau_{\zeta\zeta} = 0$ and $\tau_{\eta\zeta} = 0$ at the inner and outer boundaries are incorporated in this procedure. The diagonal matrix Λ is given by

$$\Lambda = \begin{pmatrix} 0 & 0 & 0 & 0 & 0 \\ 0 & C_p\sqrt{\zeta_y^2 + \zeta_z^2} & 0 & 0 & 0 \\ 0 & 0 & -C_p\sqrt{\zeta_y^2 + \zeta_z^2} & 0 & 0 \\ 0 & 0 & 0 & C_s\sqrt{\zeta_y^2 + \zeta_z^2} & 0 \\ 0 & 0 & 0 & 0 & -C_s\sqrt{\zeta_y^2 + \zeta_z^2} \end{pmatrix}$$

V. Results

Physical quantities are normalized with Young's modulus E, the acoustic (dilatational wave) speed C_p, and the characteristic dimension such as the inner radius of the annulus r_{in}. Young's modulus is given by $E = 2.1 \times 10^{12}$ dyne/cm^2 for the steel annulus considered here. The predictions are compared with the axisymmetric steady-state theoretical solution [30,31] for a rotating annulus.

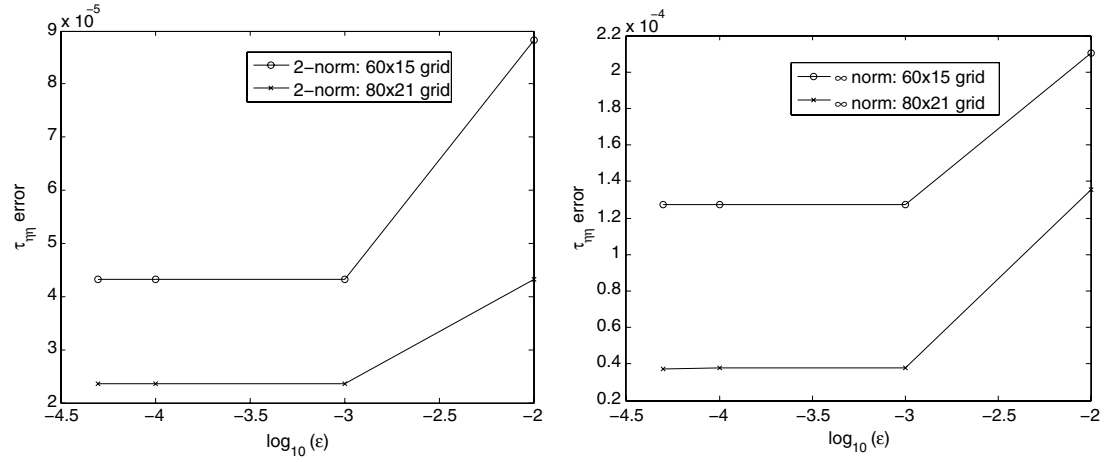

a) b)

Fig. 9 The $\tau_{\eta\eta}$ error norms as a function of dissipation parameter: a) 2-norm and b) ∞-norm.

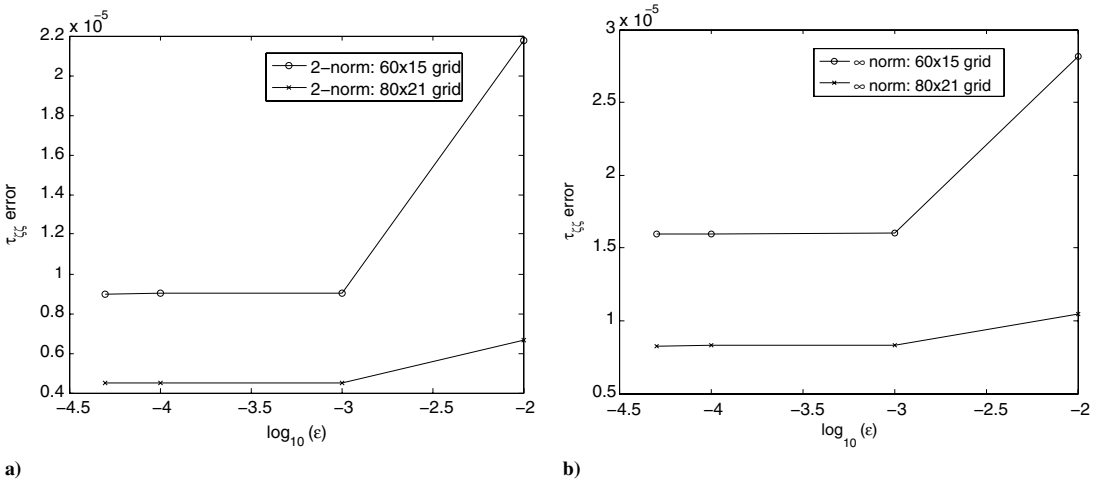

a) b)

Fig. 10 The $\tau_{\zeta\zeta}$ error norms as a function of dissipation parameter: a) 2-norm and b) ∞-norm.

A. Rotating Annulus

The thickness of the axisymmetric rotating annulus is assumed to be sufficiently small as compared with its radius so that the radial and tangential stresses do not vary over its thickness and therefore the solution sought is the plane stress solution. The closed-form plane stress solution for the rotating annulus is given in [30,31]. The weight of the annulus is neglected. An annulus with inner and outer radii of 10 and 30 cm is chosen for the simulation.

Because the theoretical solution for the rotating annulus is well established [30,31], the need for a standard grid independence study is not crucial here. During numerical simulation, it was determined that a uniform 80×21 grid yields an accurate solution. However, two representative uniform grids, 80×21 and 60×15, are chosen to demonstrate the efficacy of the scheme, with 80 or 72 points in the circumferential direction η and 21 or 15 points in the radial direction ζ, respectively. Figure 1 shows the 80×21 annulus grid. It is important to note here that the effect of the dissipation parameter on the accuracy of the solution is appreciable. Four different values of dissipation parameter equal to 0.01, 0.001, 0.0001, and 0.00005 were chosen to assess the effect of the new dissipation term on the numerical solution. The annulus results correspond to a moderate rotational speed of 100 rotations per second (rps). Initially, the annulus is at rest at a zero-stress state. As the annulus is impulsively rotated at 100 rps, it is thrown into a state of vibrations about an equilibrium configuration that it would attain, had it been rotated gradually from rest. The time history of these vibrations is followed and the eventual equilibrium state is compared with the theoretical solution [30,31].

Before discussing the results with the new scheme, a typical calculation for a 80×21 grid was carried out with the conventional dissipation term [15] using $\epsilon = 0.00005$ and the time step $\Delta t = 1.25\text{E} - 04$. The results for the normalized tangential stress $\tau_{\eta\eta}/E$ and the horizontal velocity v/C_p are shown in Figs. 2a and 2b. The solution diverges very rapidly, as shown. In fact, time steps 2 orders

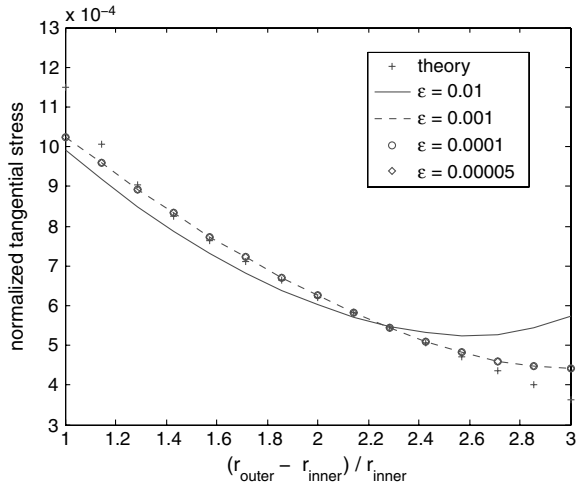

Fig. 12 Tangential stress predictions compared with theory [30,31] for various values of ϵ with the 60 × 15 grid.

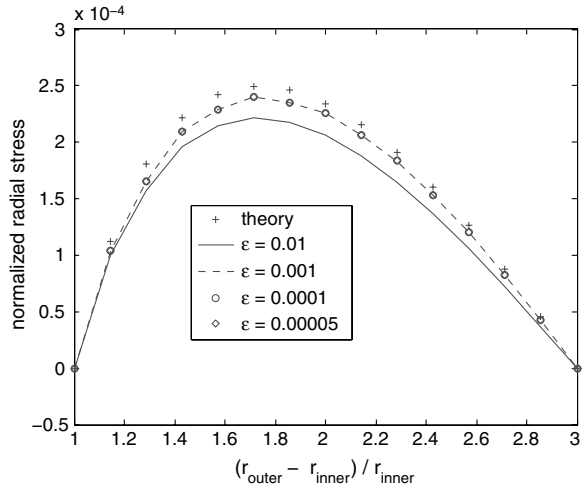

Fig. 11 Radial stress predictions compared with theory [30,31] for various values of ϵ with the 60 × 15 grid.

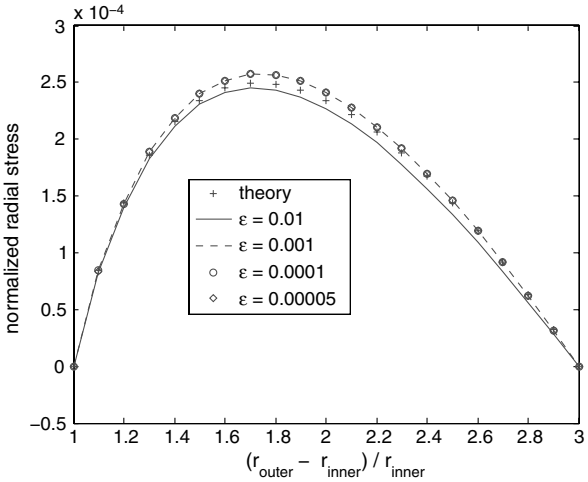

Fig. 13 Radial stress predictions compared with theory [30,31] for various values of ϵ with the 80 × 21 grid.

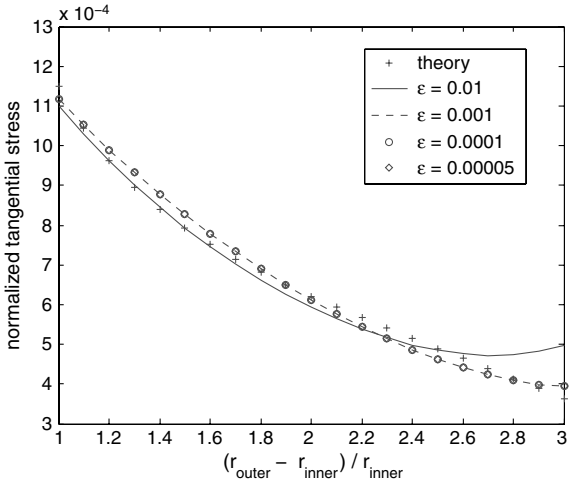

Fig. 14 Tangential stress predictions compared with theory [30,31] for various values of ϵ with the 80 × 21 grid.

of magnitude smaller than used here begin to stabilize the solution with the conventional scheme. But with the new scheme, the solution is stable and convergent for the time step used here, as we shall see subsequently.

The first simulation with the new scheme corresponds to the 80×21 grid with $\epsilon = 0.00005$ and $\Delta t = 1.25\text{E} - 04$. The time evolution up to the normalized time of 0.23 (i.e., 23 rotations of the disk) of the three quantities (tangential stress $\tau_{\eta\eta}$, radial stress $\tau_{\zeta\zeta}$, and horizontal velocity v) are shown at given radial locations along a radial line extending vertically up. The results, shown in Figs. 3a–3d, show the corresponding vibrations attenuating over time. On closer inspection of the early time histories shown in Figs. 4a–4d, the annular disk rotating at 100 rps is shown to vibrate at a natural frequency of approximately 5 KHz.

The corresponding steady-state results for $\tau_{\eta\eta}$ and $\tau_{\zeta\zeta}$ are compared with the theoretical results [30,31] in Fig. 5. The agreement between the simulations and the theory is sufficiently accurate.

The second simulation with the new scheme is a repeat of the first simulation, except that the grid for the present simulation is 60×15. Corresponding results are shown in Figs. 6a–6d, 7a–7d, and 8. Note that the natural frequency response is maintained at about 5 KHz in this simulation. With the 60×15 grid, simulation results suffer a degradation in accuracy, as expected. This is shown through the comparison with the theory in Fig. 8. Although refining the grid from 60×15 to 80×21 results in sufficient improvement in accuracy of the predictions, the effect of the dissipation parameter ϵ on the accuracy of the predictions, regardless of the grid used, is remarkable, as we shall see in the following section.

B. Accuracy and Uncertainty

In employing the artificial dissipation techniques in the solution of partial differential equations, it is customary to choose the dissipation parameter $\epsilon \ll 1$, and if the solution remains stable with this choice of ϵ, the ensuing solution is taken as acceptable. But, as we shall see subsequently, this is not acceptable in the problem studied here. Four values of ϵ equal to 0.01, 0.001, 0.0001, and 0.00005 were selected with the four corresponding stable values of Δt of $5.\text{E} - 03$, $2.5\text{E} - 03$, $2.5\text{E} - 04$, and $1.25\text{E} - 04$, respectively. The four simulations with these values of ϵ and Δt were carried out for the 60×15 grid and again for the 80×21 grid.

For both the 60×15 and 80×21 grids, the results of the steady-state error analysis are shown in Fig. 9. The error is measured with respect to the theoretical solution [30,31]. Figure 9a shows the decrease in the 2-norm of the error, and Fig. 9b shows that for the ∞-norm of the error in the tangential stress as the dissipation parameter, ϵ is decreased. Similarly, Figs. 10a and 10b show the corresponding results for the radial stress. It is observed that the relative magnitudes of these error norms are lower for the 80×21 grid, as expected, and there is a clear dependence of the solution on the dissipation

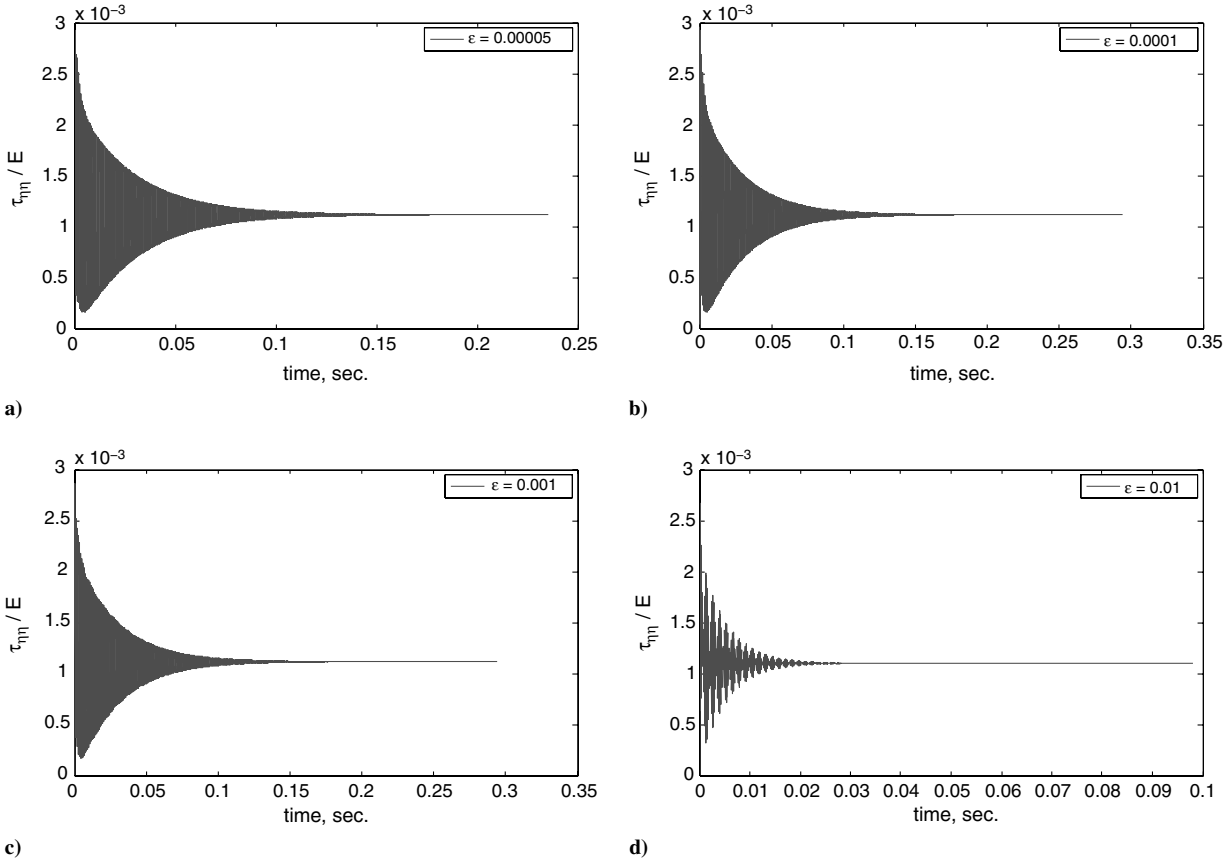

Fig. 15 Effect of dissipation on the $\tau_{\eta\eta}$ vibration attenuation at $L = 1$; annulus rotating at 100 rps; 80 × 21 grid; larger values of ϵ damp the system too rapidly.

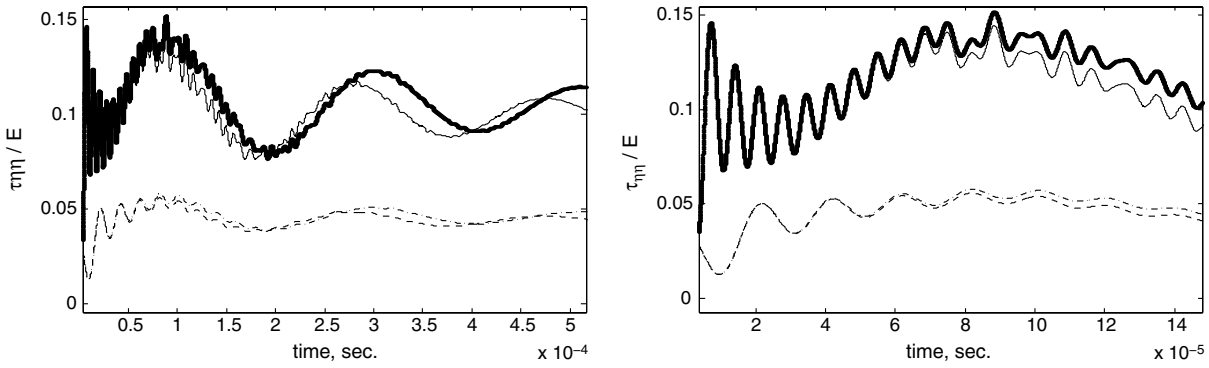

a) Initial response **b) Enlarged view of the initial response**

Fig. 16 Comparison of the $\tau_{\eta\eta}$ evolution with and without the Coriolis effect; annulus rotating at 1000 rps; $L = 1$ boundary (thick solid line), $L = 1$ without Coriolis term (thin solid line), $L = 21$ boundary (dashed line), and $L = 21$ without Coriolis term (dashed-dotted line).

parameter. It is only for values of ϵ of 0.001 and below that the solution begins to become independent of ϵ and attain the correct form.

To quantify this error, point to point, with ϵ as a parameter, Fig. 11 shows this parametric comparison for radial stress $\tau_{\zeta\zeta}$ with the four values of ϵ for the 60×15 grid. Clearly, as ϵ decreases, the predictions uniformly tend to the exact solution. Figure 12 shows the corresponding comparison for the tangential stress $\tau_{\eta\eta}$ for the 60×15 grid. Similar behavior is exhibited by the predictions.

Again, correspondingly, for the 80×21 grid, Figs. 13 and 14 exhibit similar behavior of the error. In this case, as ϵ is decreased, the predictions tend to the exact solution more closely because the grid is finer.

An interesting result in Figs. 15a–15d shows that as ϵ is increased, the solution, chosen here as $\tau_{\eta\eta}$, is overdamped with $\epsilon = 0.01$, and the vibrations attenuate too quickly, eventually leading to an inaccurate solution.

Finally, another simulation was carried out for the case of a high rate of rotation of 1000 rps, and a comparison between results for tangential stress $\tau_{\eta\eta}$ with and without the Coriolis force term in the governing equations was made. The solution without the Coriolis term is incorrect in the noninertial frame of reference, but the comparison shown here serves to identify the magnitude of the Coriolis effect. The results are shown in Figs. 16a and 16b. The long-time frequency response of 5 KHz is maintained as in the case of 100 rps, as shown in Fig. 16a. Figure 16b shows the tangential stress vibration response immediately following the impulsive start to be very high: approximately 150 KHz at the inner boundary and 50 KHz at the outer boundary. This short-lived secondary frequency response is superimposed on the long-time natural frequency response of 5 KHz. For moderate rotation of 100 rps, this additional initial high-frequency content is absent. The effect of Coriolis force manifests itself following a very short interval after initial start and, not shown here, persists until the steady state is achieved, as expected.

VI. Conclusions

A new first-principles formulation in noninertial frame and in generalized curvilinear coordinates to study the elastodynamics of bodies of nonuniform material properties in rotation has been presented. A new dissipative time-centered leapfrog scheme is proposed here that has enhanced stability characteristics over the conventional dissipative leapfrog scheme. The new scheme has been incorporated in the elastodynamic simulator FiDDLE to generate the predictions. The axisymmetric predictions, obtained directly in the time domain with the new formulation, and the new numerical scheme are validated by comparing them with a steady-state axisymmetrical theoretical solution [30,31].

The scheme can readily be applied to bodies with nonuniform material properties for use in wave-based SHM and fluid–structure interaction (FSI) problems, without any special boundary treatment needed at material interfaces. Using the proposed formulation, of particular use is the one-to-one correspondence of the grids on the fluid–structure grid interfaces that obviates the need for solution interpolation back and forth between the fluid and structure solutions at these interfaces for FSI applications with traditional approaches. The present approach coupled with a finite difference computational fluid dynamics methodology can be extended easily in a pure Lagrangian fashion to track the evolving fluid–structure interface in a given FSI application. Reference signatures with and without material damage can be obtained directly in the time domain with the present approach and used for damage detection in SHM applications [24,25].

Acknowledgment

This work was funded by the Supersonics Project of the NASA Fundamental Aeronautics Program.

References

[1] Virieux, J., "SH-Wave Propagation in Heterogeneous Media: Velocity-Stress Finite Difference Method," *Geophysics*, Vol. 49, No. 11, Nov. 1984, pp. 1933–1957. doi:10.1190/1.1441605

[2] Madariaga, R., "Dynamics of an Expanding Circular Fault," *Bulletin of the Seismological Society of America*, Vol. 66, June 1976, pp. 639–666.

[3] Virieux, J., "P-SV Wave Propagation in Heterogeneous Media: Velocity-Stress Finite Difference Method," *Geophysics*, Vol. 51, No. 4, 1986, pp. 889–901. doi:10.1190/1.1442147

[4] Pitarka, A., "A 3-D Elastic Finite Difference Modeling of Seismic Motion Using Staggered Grids with Nonuniform Spacing," *Bulletin of the Seismological Society of America*, Vol. 89, Feb. 1999, pp. 54–68.

[5] Graves, R., "Simulating Seismic Wave Propagation in 3D Elastic Media Using Staggered-Grid Finite Differences," *Bulletin of the Seismological Society of America*, Vol. 86, No. 4, 1996, pp. 1091–1106.

[6] Schroeder, C. T. S., and Scott, W. R., Jr., "A Finite Difference Model to Study Elastic-Wave Interactions with Buried Land Mines," *IEEE Transactions on Geoscience and Remote Sensing*, Vol. 38, No. 4, 2000, pp. 1505–1512. doi:10.1109/36.851950

[7] Sigalas, M. M., and Garc, N., "A Theoretical Study of Three Dimensional Elastic Band Gaps with the Finite Difference Time-Domain Method," *Journal of Applied Physics*, Vol. 87, No. 6, 2000, pp. 3122–3125. doi:10.1063/1.372308

[8] Lombard, B., and Piraux, J., "How to Incorporate the Spring-Mass Conditions in Finite Difference Schemes," *SIAM Journal on Scientific Computing*, Vol. 24, No. 4, 2003, pp. 1379–1407. doi:10.1137/S1064827501385931

[9] Lombard, B., and Piraux, J., "Numerical Modeling of Elastic Waves Across Imperfect Contacts," *SIAM Journal on Scientific Computing*, Vol. 28, No. 1, 2006, pp. 172–205. doi:10.1137/05062740X

[10] Moczo, P., Kristek, J., Vavrycuk, V., Archuleta, R. J., and Halada, L., "3D Heterogeneous Staggered-Grid Finite Difference Modeling of Seismic Motion with Volume Harmonic and Arithmetic Averaging of

Elastic Moduli and Densities," *Bulletin of the Seismological Society of America*, Vol. 92, No. 8, 2002, pp. 3042–3066.
doi:10.1785/0120010167

[11] Zhang, J., "Quadrangle Grid Velocity Stress Finite Difference Method for Elastic Wave Propagation Simulation," *Geophysical Journal International*, Vol. 131, Apr. 2007, pp. 127–134.

[12] Kaul, U. K., "FiDDLE: A Computer Code for Finite Difference Development of Linear Elasticity in Generalized Curvilinear Coordinates," NASA TM-2005-213450, 2005.

[13] Kaul, U. K., "Modeling and Simulation of Normal and Damage Vibration Signatures of Idealized Gears," *Structural Health Monitoring*, Vol. 8, No. 1, 2009, pp. 17–28.
doi:10.1177/1475921708094791

[14] Kaul, U. K., "Finite Difference Modeling and Simulation of Idealized Gear Vibrations," *Proceedings of the 5th International Workshop on Structural Health Monitoring*, DEStech, Lancaster, PA, 12–14 Sept. 2005, p. 1183.

[15] Press, W. H., Teukolsky, S. A., Vetterling, W. T., and Flannery, B. P., *Numerical Recipes in C*, Cambridge Univ. Press, New York, 1999.

[16] Kaul, U. K., "Finite Difference Simulation and Visualization of Elastodynamics in Time-Evolving Generalized Curvilinear Coordinates," U.S. Patent, Filed 19 Jan. 2006, NASA Case No. ARC-15462-1.

[17] Kaul, U. K., "New Boundary Constraints for Elliptic Systems Used in Grid Generation Problems," *Journal of Computational Physics*, Vol. 189, No. 2, 2003, pp. 476–492.
doi:10.1016/S0021-9991(03)00229-8

[18] Kaul, U. K., "Enhanced Elliptic Grid Generation," U. S. Patent 7231329, 12 June 2007.

[19] Chang, F. K., "SHM Design for Space Operation Vehicles," *First International Forum on Integrated System Health Engineering and Management in Aerospace (ISHEM 2005)*, NASA, 7–10 Nov. 2005.

[20] Ha, S., and Chang, F. K., "A Review of Energy Harvesting Methodologies for Potential Structural Health Monitoring Applications," *Proceedings of the 5th International Workshop on Structural Health Monitoring*, DEStech, Lancaster, PA, 12–14 Sept. 2005, p. 1451.

[21] Park, J., and Chang, F. K., "Built-In Detection of Impact Damage in Multi-Layered Thick Composite Structures," *Proceedings of the 4th International Workshop on Structural Health Monitoring*, DEStech, Lancaster, PA, 15–17 Sept. 2003, p. 1391.

[22] Giurgiutiu, V., and Yu, L., "Comparison of Short-Time Fourier Transform and Wavelet Transform of Transient and Tone Burst Wave Propagation Signals for Structural Health Monitoring," *Proceedings of the 4th International Workshop on Structural Health Monitoring*, DEStech, Lancaster, PA, 15–17 Sept. 2003, p. 1267.

[23] Jata, K. V., and Parthasarathy, T. A., "Physics of Failure," *First International Forum on Integrated System Health Engineering and Management in Aerospace (ISHEM 2005)*, NASA, 7–10 Nov. 2005.

[24] Kaul, U. K., and Oza, N., "Machine Learning for Detecting and Locating Damage in a Rotating Gear," *SAE 2005 Transactions: Journal of Aerospace*, Vol. 114, No. 1, Feb. 2006, pp. 1198–1202; also Society of Automotive Engineers, Paper 2005-01-3371, 2005.

[25] Kaul, U. K., "Idealized Modeling and Analysis of the Shuttle Orbiter Wing Leading Edge Impact," *SAE 2005 Transactions: Journal of Aerospace*, Vol. 116, May 2008; also Society of Automotive Engineers, Paper 2007-01-3882, 2007.

[26] Chandrasekhar, S., *Hydrodynamic and Hydromagnetic Stability*, Dover, New York, 1981.

[27] Kaul, U. K., and Shreeve, R. P., "Full Viscous Modeling in Generalized Coordinates of Heat Conducting Flows in Rotating Systems," *Journal of Thermophysics and Heat Transfer*, Vol. 10, No. 4, 1996, pp. 621–626.
doi:10.2514/3.838

[28] Viviand, H., "Conservative Forms of Gas Dynamic Equations," *La Recherche Aérospatiale*, No. 1974-1, 1974, pp. 65–68.

[29] Kaul, U. K., "An Improved Dissipative Leap-Frog Finite Difference Scheme for Elastodynamic Simulation," NASA, TM-2008-215360, Aug. 2008.

[30] Timoshenko, S. P., and Goodier, J. N., *Theory of Elasticity*, McGraw–Hill, New York, 1934.

[31] Love, A. E. H., *The Mathematical Theory of Elasticity*, Dover, New York, 4th ed., 1944.

R. Ohayon
Associate Editor